



ORIGINAL ARTICLE

Development of a biocompatible green drug release system using salidroside-TiO₂-doped chitosan oligosaccharide molecularly imprinted polymers



Zijie Liu ^{a,1}, Xingbin Ma ^{a,1,*}, Shuyu Li ^a, Jiajie Qiu ^a, Siyu Liu ^a, Zhifeng Huang ^a, Hongling Lin ^b, A.M. Abd El-Aty ^{c,d,e}

^a College of Coastal Agricultural Sciences, Guangdong Ocean University, Zhanjiang 524088, Guangdong, China

^b Zhanjiang Experimental Station, Southern-Subtropical Crop Research Institute, Chinese Academy of Tropical Agricultural Sciences, Zhanjiang 524013, China

^c Department of Pharmacology, Faculty of Veterinary Medicine, Cairo University, 12211 Giza, Egypt

^d State Key Laboratory of Biobased Material and Green Papermaking, Qilu University of Technology, Shandong Academy of Sciences, Jinan, 250353, China

^e Department of Medical Pharmacology, Medical Faculty, Ataturk University, 25240 Erzurum, Turkey

Received 30 April 2023; accepted 1 July 2023

Available online 6 July 2023

KEYWORDS

Surface molecularly imprinted polymer;
Salidroside;
Novel functional monomer;
Diethylene glycol dimethacrylate;
Sustained release

Abstract This study focuses on creating a green drug release system using a food-grade titanium dioxide (TiO₂) material through surface molecular imprinting. Salidroside (SD) was chosen as the template molecule to synthesize molecularly imprinted polymers (SDT-MIP) utilizing TiO₂-doped chitosan oligosaccharides as the functional monomer. The SDT-MIPs were characterized using multiple techniques, and their effectiveness was evaluated through an *in vitro* release study. Additionally, the affinity of SDT-MIPs toward the template molecule was examined using Langmuir and Freundlich adsorption models. The Langmuir model revealed a maximum capacity of 170.41 mg/g and an imprinted factor of 3.4. The study demonstrated that drug release from the SDT-MIPs in simulated gastrointestinal fluid primarily occurred through pure Fick diffusion. The release kinetics exhibited diffusion coefficients ranging from $3.38 \times 10^{-3} \text{ cm}^2/\text{s}$ to $2.78 \times 10^{-2} \text{ cm}^2/\text{s}$, indicating their biocompatibility and potential application in drug delivery. Furthermore, the SDT-MIP demonstrated no adverse impact on cell viability even at concentrations as high as 1000 $\mu\text{g}/\text{mL}$. The survival rate of cells cultivated in the presence of SDT-MIP solution exceeded $120 \pm 12.46\%$.

* Corresponding author.

E-mail addresses: mxb1984612@126.com (X. Ma), abdely44@hotmail.com (A.M. Abd El-Aty).

¹ Xingbin Ma and Zijie Liu contributed equally to this paper.

Peer review under responsibility of King Saud University.



providing evidence of the excellent biocompatibility and absence of cytotoxicity associated with SDT-MIP. The SDT-MIP possesses favorable sustained-release properties and lacks toxicity, allowing novel drug delivery systems to be created.

© 2023 Guangdong Ocean University. Published by Elsevier B.V. on behalf of King Saud University. This is an open access article under the CC BY-NC-ND license (<http://creativecommons.org/licenses/by-nc-nd/4.0/>).

1. Introduction

Surface molecularly imprinted polymers (SMIPs) have recognition sites located on the surface of the polymer or solid phase matrix, which simplifies their manufacturing process compared to traditional molecularly imprinted polymers (MIPs). The surface location of the recognition sites in SMIPs provides several advantages, such as improved recognition selectivity, higher binding capacity, and improved reaction efficiency (Liang et al., 2019). This positioning helps overcome some of the limitations of MIP, such as compensating for template molecules that are deeply embedded in the polymer matrix or difficult to elute and addressing the uneven distribution of recognition sites in MIP (Ma et al., 2018). The unique combination and selection of characteristics in SMIPs have attracted significant research attention across multiple fields. SMIPs have been found to be useful in solid-phase extraction of specific target molecules (Ma et al., 2022), chromatographic separation (Ma et al., 2020), drug delivery systems for sustained release of drugs (Yuksel and Tektas 2022), environmental detection (Bai et al., 2022), and chemical composition enrichment and separation (Ma et al., 2019a, 2019b). An efficient and reliable method for synthesizing MIPs with high selectivity and specificity for the target molecule is crucial. It is also important to ensure the stability and durability of MIPs and their compatibility with different biological environments, particularly in drug delivery systems. Optimization of the imprinting process, including the selection of the template molecule, functional monomer, and polymerization conditions, is essential for successful MIP applications in various fields. Developing new functional monomers and enhancing imprinting techniques are necessary for the practical application of molecular imprinting technology, especially in the pharmaceutical industry. The specific recognition and selective adsorption capabilities of MIPs make them excellent drug carriers, and their ability to delay drug release and increase drug loading can significantly enhance patient compliance and treatment efficacy (Karthika et al., 2018). Among them, molecularly imprinted polymer microspheres have gained widespread use due to their various benefits, including high selectivity, uniform particle size, and good dispersion. Molecular imprinting technology has also been combined with hydrogel materials to produce molecularly imprinted hydrogel microspheres that offer significant advantages, such as improved drug release and increased drug loading (Bakhshizadeh et al., 2017). In addition, the specific recognition ability of molecularly imprinted polymers can also be applied in the development of targeted drugs. Specifically, MIPs can be synthesized using specific receptors on body tissues or cells as template molecules (Vaneckova et al., 2020). These MIPs can selectively recognize the corresponding receptors in the body (Wang et al., 2022) and subsequently release drugs upon binding to the receptors, meeting the requirements of targeted drug delivery.

TiO₂, particularly its anatase form, is a widely used material due to its low cost, environmental friendliness, and high photocatalytic activity. This has led to its potential use in various applications, such as photocatalytic degradation of pollutants, antimicrobial agents, and drug delivery systems (Shklover et al., 1997). However, its selectivity can be improved by methods such as doping, surface modification, or adding a metal (Zhu et al., 2019). For drug delivery applications, TiO₂ and its complexes have demonstrated high efficiency as drug carriers (Zheng et al., 2019). Enhancing the adsorption of the complex is essential for improving release efficiency (Salahuddin et al., 2021). By combining TiO₂ and its composite with MIP, researchers have created

molecularly imprinted TiO₂ and its composite, which exhibit excellent photoelectric performance (Al-Nemrawi et al., 2022) and improved selectivity. This combination can coexist with a variety of drugs in the system (Hasanzadeh Kafshgari et al., 2019) and can increase the antibacterial properties and degradation efficiency of drugs (Lee et al., 2021). A hydrothermal silica etching method was successfully employed to synthesize TiO₂ hollow spheres with controllable sizes. Notably, the SiO₂ cores could be easily removed without the use of any toxic reagents. This process further confirms that the resulting hollow TiO₂ material is relatively safe for medical applications (Di and Yong-guang, 2019). Chitosan, a natural polysaccharide, offers numerous advantages, such as nontoxicity, biodegradability, excellent biocompatibility, and wide availability. Chitosan oligosaccharides, which are partially deacetylated products, have found extensive usage in medicine, biology, and other related fields (Ailincui et al., 2022). These materials effectively improve the release systems and expand the application range of TiO₂ and its composites with MIP.

Salidroside has drawbacks, such as a short half-life, rapid metabolism, wide variation in blood concentration, and low bioavailability (He Lili and Yunzhu, 2013). Although it is highly soluble in water, conventional slow and controlled-release nanoparticles have low encapsulation efficiency (Luo et al., 2015). Salidroside is mainly administered in oral dosage forms, which can cause gastrointestinal reactions related to the drug's cholinergic activity (Zhong et al., 2010). To reduce side effects and improve patient compliance, developing a better dosage form is a popular research direction (Ceglowski et al., 2022, Zhang et al., 2022). Sustained and controlled-release drug delivery systems are being investigated to reduce the frequency of administration and fluctuations in blood concentration. Molecularly imprinted microspheres present a hopeful solution as drug carriers, providing advanced formulations for sustained and controlled drug release. This offers the potential to enhance patient convenience and compliance.

This study combines biocompatible TiO₂ microspheres with molecular imprinting technology, utilizing the common structural properties of their active compounds. A series of SDT-MIPs were synthesized through precipitation polymerization. The drug loading and release mechanisms were analyzed, and the molecular recognition mechanism of the polymer was investigated. The most favorable synthesis system for SDT-MIPs was selected to develop slow-release microspheres with high molecular recognition capability, class specificity, and selectivity. Various techniques, including scanning electron microscopy (SEM), X-ray diffraction (XRD), transmission electron microscopy (TEM), and Fourier transform infrared spectroscopy (FT-IR), were employed to confirm the successful synthesis of SDT-MIP on the surface of TiO₂-chitosan oligosaccharide nanoparticles (TiO₂-COS). The aim was to create a drug carrier with desirable characteristics, such as enhanced drug loading, controlled drug release, oral administration safety, and *in vitro* drug stability. Additionally, the improved drug loading capacity of molecularly imprinted polymers introduces a novel approach for medication delivery.

2. Experimental

2.1. Materials

Chitosan oligosaccharide (molecular weight: ≤ 3000 Da; polymerization degree is approximately 160; degree of acetylation

is 90%) was provided by Shanghai Yuanye Bio-Technology Co., Ltd. (Shanghai, China). TiO_2 (average pore size 100–300 nm), sodium dodecyl sulfate (SDS), and (3-aminopropyl)-trimethoxysilane (APS) were purchased from Aladdin (Shanghai, China). N-Hydroxy succinimide (NHS), 1-ethyl-3-(two methyl-aminopropyl)-carbon (EDC), diethylene glycol dimethacrylate (EGDMA), and azobisisobutyronitrile (AIBN) were obtained from Alfa Aesar (Heysham, UK). Salidroside (purity > 98%) was obtained from Chengdu Ruiphens Biotechnology Co., Ltd. (Chengdu, China). Intestinal pig epithelial cells (IPEC-J2) were obtained from Guoqiang Zhu of China Yangzhou University. All other materials were of analytical reagent grade and acquired from Beijing Chemical Reagent Factory (Beijing, China).

2.2. Instruments and chromatography

Characterization of the polymers was performed using Fourier transform infrared spectroscopy (FT-IR), employing the attenuated total reflection (ATR) technique with a diamond crystal material. The measurements were carried out using a PU9800 instrument from PANalytical, based in Almelo, The Netherlands. The selectivity and affinity of a molecularly imprinted polymer (MIP) were assessed using high-performance liquid chromatography (HPLC) with an Agilent Infinity II 1260 system (Agilent, Waldbronn, Germany) and a PAD detector set to operate at 274 nm. Separation was achieved on a C18 column (COSMOSIL C18; 2.1 mm \times 150 mm, 5 μm) obtained from Nacalai Tesque (Kyoto, Japan) and maintained at 30 $^\circ\text{C}$. The mobile phase comprised acetonitrile (A) and ultrapure water (B), and the injection volume was 60 μL with a flow rate of 1 mL/min.

Scanning electron microscopy images were captured with a Gemini-300 scanning electron microscope (Zeiss, Oberkochen, Germany) at 3 kV. Transmission electron microscopy images were taken with a JEM-2100F transmission electron microscope (JEOL, Tokyo, Japan) at 200 kV. The X-ray diffraction patterns were obtained using a D8-Advance (Bruker, Germany). The following equipment was utilized: Miller-Q ultrapure water filter (Milli hole), 1/10,000 electronic balance (Mettler, Switzerland), low-temperature high-speed centrifuge (Thermo Technologies) and Milli-Q ultrapure water machine (Milli-Q, France).

2.3. Preparation of $\text{TiO}_2@OH$

Following the procedures outlined in previous research, 20.00 g TiO_2 was utilized and activated by heating at 373 K for 12 h. After activation, it was immersed in a solution of 3.0 mol/L HNO_3 at room temperature for 18 h. The resulting product was suction-filtered using a circulating water multi-purpose vacuum pump, washed with ultrapure water until neutral, eluted with 98% methanol, and then vacuum (-0.09 MPa) and dried at 333 K for 8 h to obtain $\text{TiO}_2@OH$. The sample was sealed and stored for subsequent use.

2.4. Preparation of $\text{TiO}_2@SiO_2-NH_2$

The Si-OH-containing treatment solution was obtained by adding 50 mL of 95% ethanol to the mixture, adjusting the pH to 4.5–5.5 with acetic acid, slowly adding 1 mL of APS,

and stirring well. The mixture was left to hydrolyze for 5 min. Next, 10.00 g $\text{TiO}_2@OH$ was dispersed in 50 mL of 10% hydrochloric acid solution and ultrasonicated. The mixture was refluxed at 353 K for 4 h and subsequently washed multiple times with ethanol and ultrapure water. The obtained mixture was then vacuum-dried at 353 K to yield solid materials. Next, the solids were dispersed in 50 mL of acetonitrile using ultrasonic treatment. To this dispersion, 6 mL of a solution containing Si-OH was added. The reaction system was then purged with nitrogen gas and sealed for a reaction duration of 5 h. Finally, the resulting mixture was vacuum-dried at 353 K, resulting in a solid material weighing 7.75 g, corresponding to a yield of approximately 77.46%. This solid material is referred to as $\text{TiO}_2@SiO_2-NH_2$.

2.5. Preparation of TiO_2 -chitosan oligosaccharide microspheres

The method described in (Karzar Jeddi and Mahkam 2019) was used to prepare water-soluble TiO_2 -chitosan oligosaccharide microspheres (TiO_2 -COS). Chitosan oligosaccharide (approximately 0.30 g) was gradually added to 300 mL of 2% acetic acid solution, followed by the addition of 5 mL of Span-80 and stirring at low speed for 30 min until it was fully soluble, resulting in a chitosan-oligosaccharide suspension. Next, 0.30 g of $\text{TiO}_2@SiO_2-NH_2$ powder was added to the suspension and stirred constantly for 1 h. Then, 1 mL of 20% SDS was added and mixed thoroughly, and the pH was adjusted with 0.5 mol/L HCl to 6.0–6.5 with stirring for an additional hour. Following the completion of the reaction, the mixture underwent centrifugation. The supernatant was discarded, and the resulting precipitate was collected. Subsequently, the collected precipitate was vacuum-dried at 353 K under a pressure of -0.09 MPa. The dried solid material weighed 0.48 g, corresponding to a yield of approximately 79.33%. These solid materials are identified as TiO_2 -COS-microspheres.

2.6. Synthesis of SDT-MIP

To synthesize the molecularly imprinted polymers, precipitation polymerization was employed. The 0.30 g of TiO_2 -COS-microspheres prepared in the previous step were dispersed in 30 mL of acetonitrile using ultrasonication. Next, a solution containing 1 mL (10 mg/mL) of salidroside, 15 μL of EDC, and 5 mg of NHS was prepared, shaken, and stored at 4 $^\circ\text{C}$ for 30 min before prepolymerization. Then, 0.3 mL of EDGMA was added sequentially and dissolved using ultrasonication. After nitrogen gas was added, the mixture was sealed and stored in a water bath shaker at a constant temperature for 18 h. The resulting solid was then cooled to room temperature and subjected to suction filtration. It was washed several times in succession with acetonitrile, tetrahydrofuran, and acetone, and finally, 0.14 g of salidroside- TiO_2 -MIP (SDT-MIP) was obtained (with a yield of approximately 45.87%) after vacuum (-0.09 MPa) drying at 353 K.

2.7. Study on the swelling and drug loading properties of SDT-MIP

2.7.1. Swelling capacity

To investigate the difference in hydrophilicity between SDT-MIP and SDT-NIP, the swelling capacity of the polymer in

an aqueous solution was evaluated. First, specific masses of SDT-MIP and SDT-NIP were weighed accurately and placed into a clean solid-phase extraction column (5 mL). The total mass was then measured, and the column was washed with 0.9% NaCl solution at room temperature (1 mL/min). Excess solution was removed by applying appropriate pressure. The column was subsequently dried at room temperature, and the mass was recorded every 30 min. The swelling ratio (SR) was calculated using the following formula:

$$SR = \frac{W_t - W_0}{m} \times 100\% \quad (1)$$

where W_t is the mass of the polymer at time t after swelling, W_0 is the mass of the initial polymer, and m is the mass of the weighed polymer.

2.7.2. Drug loading performance

The experimental procedure was similar to the polymer adsorption performance test, except that ultra-pure water was used as the adsorption environment. A centrifuge tube was filled with 1 mL of aqueous salidroside solution of varying concentrations (50, 100, 200, 400, 600, and 1000 $\mu\text{g/mL}$). SDT-MIP (2 mg) was added, thoroughly shaken, and placed in an oscillator at room temperature and 120 rpm for 2 h. The mixture was allowed to stand for 10 min before centrifugation at high speed (9000 r/min). The supernatant was collected, passed through a 0.22- μm filter, and analyzed using HPLC. SDT-NIP was analyzed in the same manner. All experiments were performed in triplicate, and the average values were calculated. The adsorption capacity Q (mg/g) was determined using the following equation:

$$Q = \frac{(C_0 - C_e)}{m} \times V \quad (2)$$

where C_0 is the initial concentration, C_e is the concentration of the solution after adsorption, V is the volume of the solution, and m is the mass of the polymer.

In this experiment, the data were fitted using the Langmuir (3) and Freundlich (4) adsorption models (Langmuir 1916, Zhang et al., 2014). The former is suitable for saturated and uniform adsorbents such as molecularly imprinted polymers, while the latter assumes that adsorption takes place on heterogeneous surfaces and that there is an interaction between the adsorbed molecules. The following formulas were used:

$$Q = \frac{AC_e}{(K + C_e)} \quad (3)$$

where C_e is the concentration of the solution after adsorption, and A and K are constants.

$$Q = KC_e^n \quad (4)$$

where C_e is the solution concentration after adsorption, K is a constant, and n is the adsorption index.

The selectivity of the polymer was evaluated using the imprinting efficiency (I_e) in this experiment, which was calculated using the following formula:

$$I_e = \frac{Q_{MIP}}{Q_{NIP}} \quad (5)$$

where Q_{MIP} and Q_{NIP} represent the respective adsorption capacities.

2.8. In vitro sustained release performance evaluation and kinetic fitting

2.8.1. Artificial gastric fluid (AGF) and artificial intestinal fluid (AIF) preparation

First, 7.0 mL of 36.5% HCl and 2.0 g of NaCl were dissolved in a suitable amount of ultrapure water. The solution was then brought to a volume of 1000 mL and mixed by sonication to obtain AGF. For AIF, 0.1 g KCl, 4.0 g NaCl, 3.4 g KH_2PO_4 , and 0.72 g Na_2HPO_4 were dissolved in 400 mL ultrapure water. The resulting solution was sonicated and mixed with 0.5 mol/L HCl to achieve a pH of 7.4.

2.8.2. In vitro sustained release

Fifty milligrams of the previously prepared SDT-MIP was placed in 10 mL of either AGF (pH = 1.5) or AIF (pH = 7.4) and shaken thoroughly in a constant temperature water bath shaker at 37 °C and 180 rpm. The system was then sampled at 1, 2, 3, 4, 5, and 6 h and at 1, 3, 6, 9, 18, 24, 30, and 36 h by centrifuging 1 mL of the supernatant and adding 1 mL of fresh AGF or AIF to continue the experiment.

2.8.3. Evaluation of sustained release effect

A salidroside standard with a concentration of 1 mg/mL was obtained by reconstituting in acetonitrile. HPLC was used for analysis under the following conditions: column temperature of 30 °C; flow rate of 1 mL/min with 60% acetonitrile (A) and 40% ultrapure water (B); and detection at 275 nm. To establish a standard curve, salidroside was determined at five different concentrations (50, 100, 200, 400, 600, 800, and 1000 mg/L), and the peak area was recorded. The supernatant was then centrifuged at 2.8.2 and filtered using a syringe filter (0.45 μm) before determining the salidroside content by HPLC. All experiments were carried out in triplicate, and the results were averaged. The cumulative percent release (DS%) of salidroside was calculated as follows:

$$DS\% = \frac{M_t}{M_\infty} = \frac{V_t \sum_{i=1}^{n-1} C_i + V_o C_n}{M_\infty} \times 100\% \quad (6)$$

where V_t is the volume of the release medium at each sampling time, C_i represents the concentration of salidroside in the release medium at time i , V_o is the total volume of the release medium, C_n is the concentration of the release medium after collecting the n th sample, and M_∞ is the content of salidroside in SDT-MIP. The experiment was performed in triplicate, and the average value was used for analysis.

2.8.4. In vitro drug release kinetics

This study utilized the zero-order kinetic model (7), first-order kinetic model (8), Higuchi's plane diffusion equation (9), and the Ketger-Peppas (K-P) kinetic equations (10) to delve deeper into the drug release process of SDT-MIP and SDT-NIP and to explain their release laws and mechanisms. The Higuchi equation was used to assess whether the drug release kinetics were purely Fick diffusion release or not. Moreover, the value of n in the K-P equation could represent different release mechanisms. The threshold value for the globular structure was a pure Fick diffusion release index (n) of 0.43. For $n \leq 0.45$, pure Fick diffusion occurred, $0.45 \leq n \leq 0.89$ represented diffusion combined with the framework corrosion

mechanism, and $n \geq 0.89$ represented the framework corrosion mechanism. The corresponding model equations are as follows:

$$D_t = Kt + D_0 \quad (7)$$

where D_t is the cumulative drug release rate at time t , K is the zero-order release constant, D_0 is the initial drug concentration, and t is the release time.

$$D_t = D_\infty \left(1 - \frac{A}{D_\infty} e^{-kt} \right) = A(1 - e^{-kt}) \quad (8)$$

where D_t is the cumulative drug release rate at time t , K is the first-order release constant, D_∞ is the percent maximum cumulative release, and A is a constant.

$$S_t = Kt^{\frac{1}{2}} \quad (9)$$

where S_t is the amount of drug released at time t and K is the release rate constant.

$$D_t = K_p t^n \quad (10)$$

where D_t is the cumulative drug release rate at time t , K_p is the kinetic constant and n is the release exponent.

2.9. Cytotoxicity test

The IPEC-J2 cells were seeded in 96-well plates (density 1×10^3 cells/well) in logarithmic growth phase and treated with various concentrations of SDT-MIP (200 $\mu\text{g/mL}$, 400 $\mu\text{g/mL}$, 600 $\mu\text{g/mL}$, 800 $\mu\text{g/mL}$, and 1000 $\mu\text{g/mL}$) for 24 h. The experiment included blind control and negative control groups, and each treatment group had 6 replicates. The experiment was repeated three times, and the results were averaged. After 24 h of treatment with SDT-MIP, 10 μL CCK-8 solution was added to each well and incubated in a CO_2 incubator for 2 h. The absorbance was measured at 490 nm using a microplate reader. The cell viability (CV) was calculated as follows to determine cytotoxicity:

$$CV = \frac{G_n}{A} \times 100\% \quad (11)$$

where \bar{A} is the average value of the normal control group, and G_n is the measured value of each group.

3. Results and discussion

3.1. Synthesis of $\text{TiO}_2@/\text{NH}_2\text{-C}$ and SDT-MIP

The preparation process of SDT-MIP is illustrated in Fig. 1, which involves several key steps. First, TiO_2 was activated and modified on the surface. Second, the amination of TiO_2 was completed by the formation of O-Si bonds. Third, the numerous hydroxyl groups present on the chitosan oligosaccharide reacted with the amino groups in $\text{TiO}_2\text{-SiO}_2\text{-NH}_2$ to produce polymer spheres wrapped around TiO_2 . Finally, salidroside in $\text{TiO}_2\text{-COS}$ was subjected to the influence of cross-linkers and initiators, resulting in the creation of specific recognition sites followed by the removal of the template. The reactive silane coupling agent (3-aminopropyl)trimethoxysilane (APS) is susceptible to hydrolysis and cross-linking reactions (Kuei et al., 2015). In the presence of water, APS undergoes

hydrolysis, wherein the ethoxy group is first converted to hydroxyl groups and subsequently reacts with the hydroxyl groups present on the surface of $\text{TiO}_2\text{-OH}$, leading to the formation of an O-Si bond through dehydration (Oh et al., 2007, Zhengming et al., 2023).

3.2. Characterization and particle size determination of SDT-MIP

3.2.1. FT-IR

Fourier transform infrared spectroscopy is a useful technique for detecting and characterizing the structure of chemical substances (Jingjing et al., 2022). Fig. 2 shows the FT-IR spectra of TiO_2 , $\text{TiO}_2@/\text{NH}_2$, chitosan oligosaccharides, $\text{TiO}_2@/\text{NH}_2\text{-chitosan oligosaccharides}$, and SDT-MIP. The preparation method and ultrastructure of the materials may have caused some changes in the internal structure of the molecule, leading to the suppression of the characteristic absorption peaks of TiO_2 . The characteristic absorption peak of TiO_2 was observed at approximately 2360 cm^{-1} . Bending vibrations were observed between the H—N—H bonds in $\text{TiO}_2@/\text{NH}_2$, and a strong absorption peak was observed at approximately 1650 cm^{-1} . In the infrared spectrum of COSs, the broad peaks at approximately 3400 cm^{-1} were due to superimposed absorption peaks of hydrogen bonds, hydroxyl groups, and amino stretching vibrations within and between COSs (Shang et al., 2011, Wei et al., 2018). The absorption peaks at approximately 1620 cm^{-1} , 1515 cm^{-1} , and 1379 cm^{-1} were the amide I, amide II, and amide III bands of chitosan oligosaccharide, respectively (Cai et al., 2015, Sohan et al., 2020). The stretching vibration of the sugar ring backbone oxygen bridge (C—O—C) of chitosan oligosaccharide was observed at approximately 1095 cm^{-1} (Bo et al., 2012). The amide and oxygen bridge absorption peaks of COSs were somewhat weakened due to the binding effect of $\text{TiO}_2@/\text{NH}_2\text{-C}$. The methyl absorption peak of SDT-MIP was strengthened at approximately 2940 cm^{-1} due to the formation of a recognition site by salidroside binding. This provided initial evidence that the target product was successfully synthesized, i.e., SDT-MIP.

3.2.2. SEM and TEM

Fig. 3 displays the scanning electron microscopy (SEM) results, while Fig. 4 presents the transmission electron microscopy (TEM) results. The smooth globular-like morphology of SDT-MIP is clearly visible in Fig. 3, suggesting that the encapsulation of the target product is more successful. However, some particles appeared to stick together, which could be due to the presence of oily substances in the synthetic reagents that were not completely eluted. On the other hand, the TEM images in Fig. 4 show that the SDT-MIPs have a more regular shape and an average diameter of approximately 170 nm. The dark regions in the center correspond to the TiO_2 molecules that are wrapped by the SDT-MIP, while the brighter regions at the periphery correspond to the chitosan oligosaccharide molecules that are also wrapped around the TiO_2 core. These results further confirm the successful synthesis of the target product.

3.2.3. XRD

Fig. 5 displays the X-ray diffraction (XRD) outcomes for TiO_2 , $\text{TiO}_2@/\text{NH}_2$, $\text{TiO}_2@/\text{NH}_2\text{-COS}$, and SDT-MIP. The

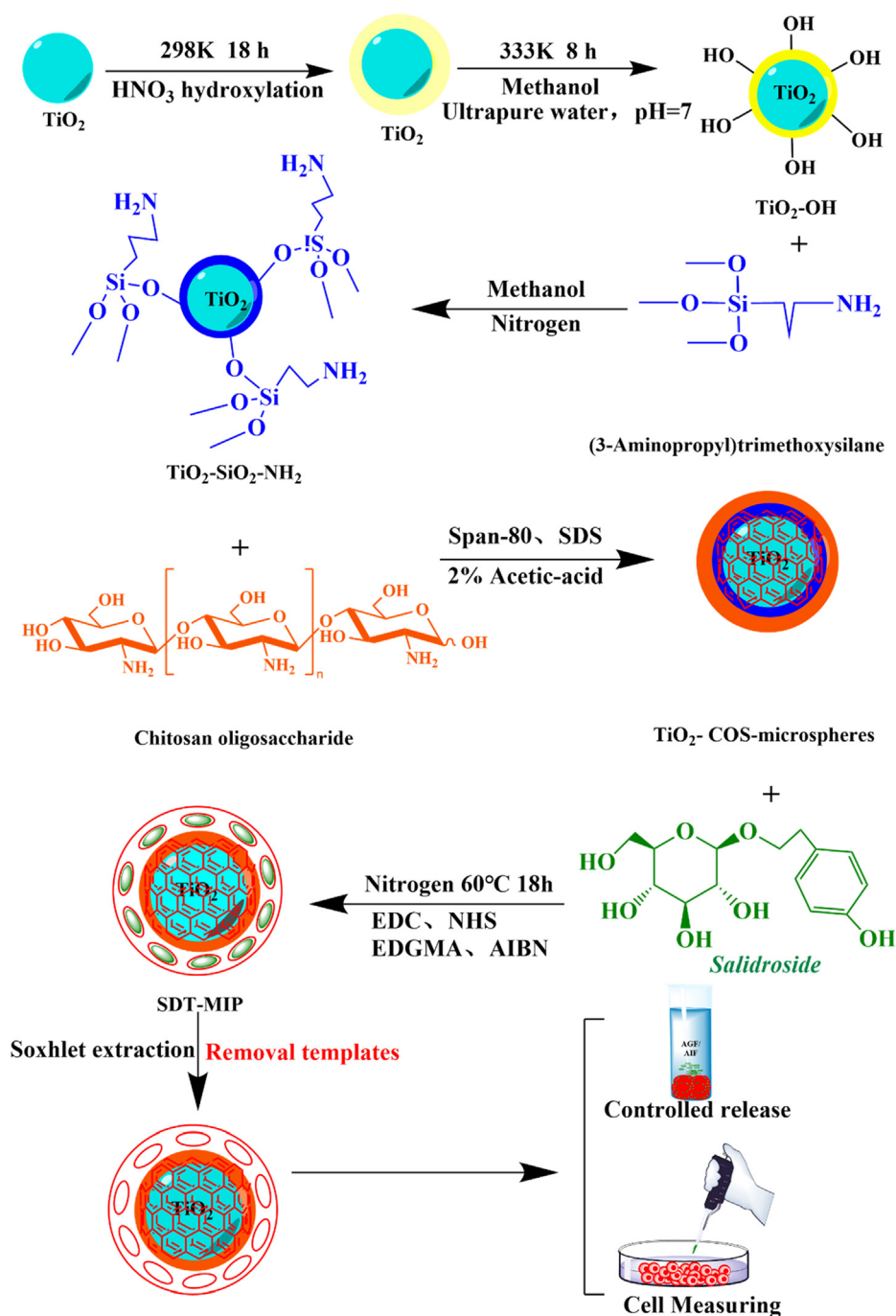


Fig. 1 Scheme representing the procedure for preparing and testing SDT-MIP.

crystallinity percentages of TiO_2 and SDT-MIP were determined to be 46.81% and 21.50%, respectively, utilizing Jade 6 software for analysis and calculation. Previous studies have shown that TiO_2 primarily exists in an anatase structure (Bakhshizadeh et al., 2017), which exhibits a strong diffraction peak at approximately 25° (1875) and three smaller peaks between 25 and 40° , as well as a diffraction peak at 47.88° (445). During the preparation of SDT-MIP, there was a gradual decrease in crystallinity, suggesting that chitosan oligosaccharides were being grafted onto TiO_2 but not fully covering its surface. These findings align with the results obtained from

FT-IR analysis, providing further confirmation of the successful synthesis of SDT-MIP.

3.3. Swelling capacity

Fig. 6 depicts the swelling behavior of SDT-MIP and SDT-NIP in an aqueous solution. Both materials exhibited an increase in swelling ratio over time, with a decreasing growth rate observed after 120 min. Notably, the swelling behavior of SDT-NIP reached a more noticeable saturation state with a gradual leveling-off trend. In contrast, the SDT-MIP, which

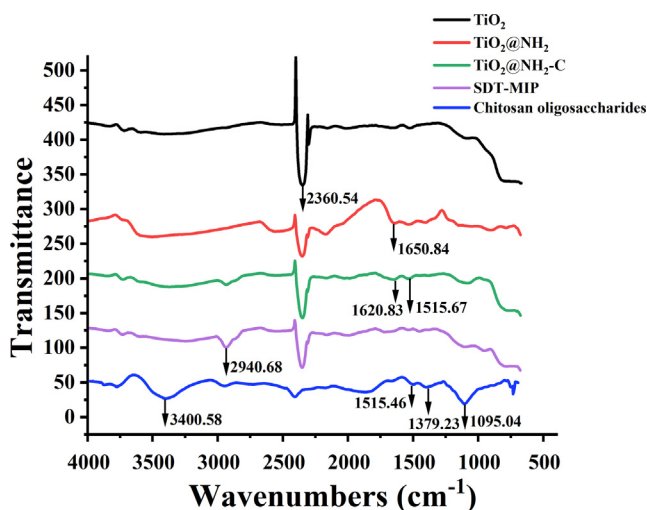


Fig. 2 FTIR spectra of TiO_2 , $\text{TiO}_2@NH_2$, $\text{TiO}_2@NH_2\text{-C}$, chitosan oligosaccharides, and SDT-MIP.

involves crosslinking between the polymer and salidroside molecule, displayed a higher swelling rate due to its ability to absorb a larger amount of solvent with higher permeability. This distinction suggests that the SDT-MIP possesses a greater potential for a larger drug adsorption area and a stronger drug loading capacity, as reported by Ma et al. (Ma et al., 2023).

3.4. Method verification of HPLC

According to the International Union of Pure and Applied Chemistry (IUPAC) recommendation and previous reports (Abbas et al., 2018, Elkins et al., 2019, Ma et al., 2019a, 2019b), the drug content was calculated using a standard curve of salidroside established in section 2.8.3. The calibration curve was good in the range of 50–1000 $\mu\text{g}/\text{mL}$ for salidroside at the seven concentration levels. The feasibility of MIP as a new slow release agent for the determination of salidroside in real samples using HPLC was evaluated in terms of linear range, correlation coefficients (R^2), limits of detection (LOD) and quantification (LOQ). The correlation coefficient was 0.9999 for salidroside by determining the standard solution, and the intraday accuracy was assessed by analyzing the same

concentration of salidroside on the same day ($n = 7$) (Yi et al., 2013). The calculated RSD ranged from 0.64 to 1.03%. The limits of detection and quantification were 3.0007 and 10.0022 $\mu\text{g}/\text{mL}$, respectively (Table 1).

3.5. Drug loading properties

Fig. 7 illustrates that SDT-MIP had better drug adsorption properties than SDT-NIP over a drug concentration range of 0–1000 $\mu\text{g}/\text{mL}$, exhibiting extremely high adsorption capacity. At a drug concentration of 1000 $\mu\text{g}/\text{mL}$, the adsorption capacity of SDT-NIP was only 50.18 mg/g, whereas that of SDT-MIP reached 170.41 mg/g. This is attributed to the presence of salidroside recognition sites on the surface of SDT-MIP, allowing for selective adsorption of more drug molecules, while SDT-NIP was only able to mechanically adsorb drug molecules due to surface molecular polarity and reticular holes formed by chitosan oligosaccharide. As shown in Fig. 8, the Langmuir and Freundlich equation models were employed and exhibited a good fitting effect, and the Langmuir model is more suitable, which indicates the saturation and homogeneity of the adsorption capacity of SDT-MIP and strong adsorption intermolecular interactions. The specific parameters of the equation are shown in Table 2. Furthermore, Fig. 9 illustrates that the imprinting efficiency of SDT-MIP increased linearly within a drug concentration range of 0–600 $\mu\text{g}/\text{mL}$, plateauing at a drug concentration of 1000 $\mu\text{g}/\text{mL}$, achieving an imprinting efficiency of 3.4. These results suggest that SDT-MIP has a strong drug loading performance within a specific drug concentration.

3.6. *In vitro* sustained release effect

The *in vitro* sustained-release behavior of SDT-MIP in artificial gastric fluid (AGF) is depicted in Fig. 10. The figure indicates that the SDT-MIP achieved the highest degree of drug release at 4 h and gradually decreased thereafter, with a slower decline indicating decomposition of the drug. Fig. 11 displays the *in vitro* sustained-release behavior of SDT-MIP in artificial intestinal fluid (AIF). The cumulative degree of drug release gradually increased with time within 24 h, with a relatively rapid increase rate in the first 1–3 h and a slow increase thereafter, indicating a good sustained-release effect. Combining the

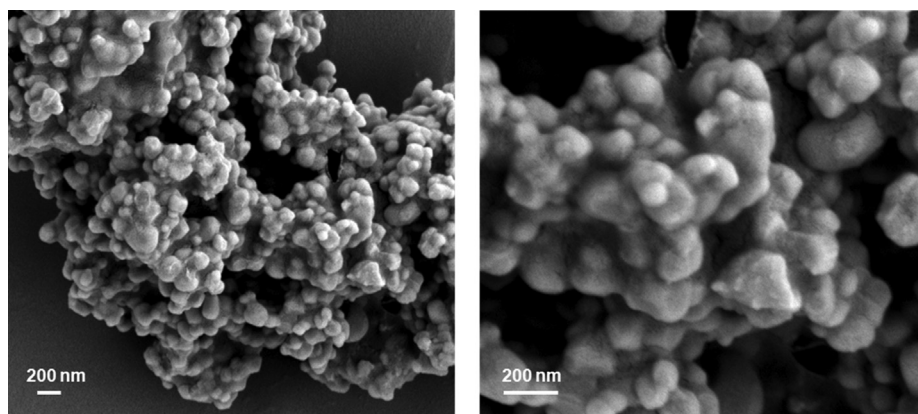


Fig. 3 Scanning electron microscopy images of SDT-MIP.

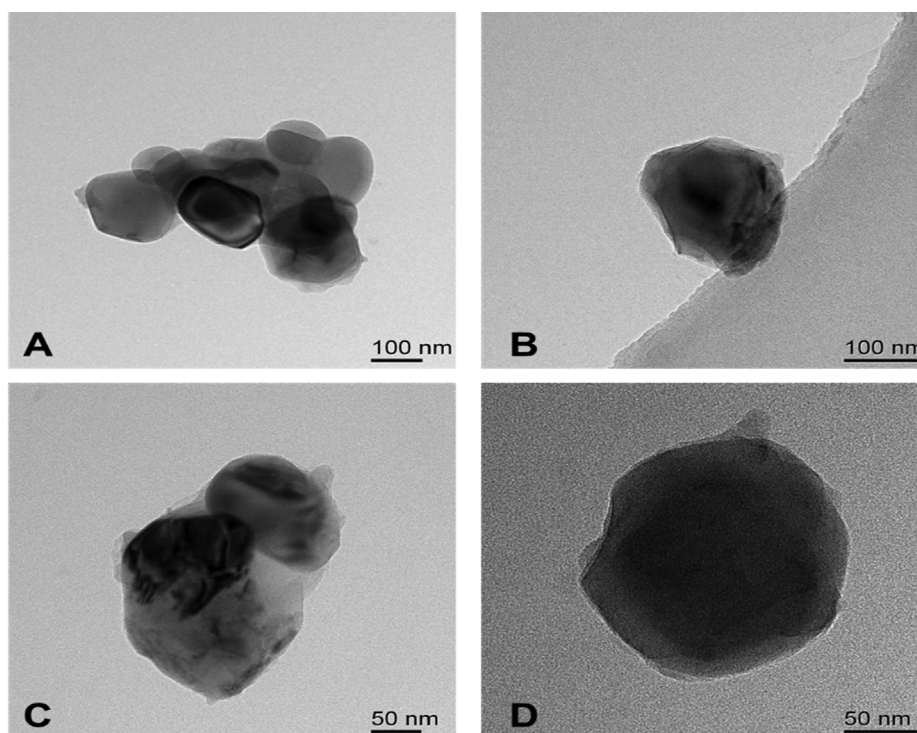


Fig. 4 Transmission electron microscopy images of SDT-MIP.

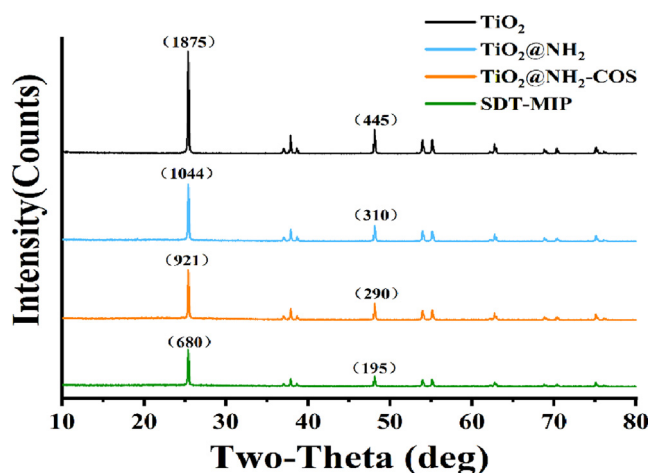


Fig. 5 X-ray diffraction results of TiO_2 , $\text{TiO}_2@NH_2$, $\text{TiO}_2@NH_2\text{-COS}$, and SDT-MIP.

results of Fig. 10 and Fig. 11, it can be concluded that the peak of the cumulative degree of drug release in AGF was much larger than that in AIF. The drug concentrations released by SDT-MIP in artificial intestinal fluid (AIF) and artificial gastric fluid (AGF) were measured using high-performance liquid chromatography (HPLC) at different time intervals. Fig. 12 illustrates that the drug release performance of SDT-MIP in AIF was considerably superior to that in AGF. The authors suggested that the acidic environment and lower pH of gastric fluid may have damaged the structure of SDT-MIP, leading to rapid drug release in the first 4 h, whereas the weakly basic pH of intestinal fluid was more conducive to a slow-release effect.

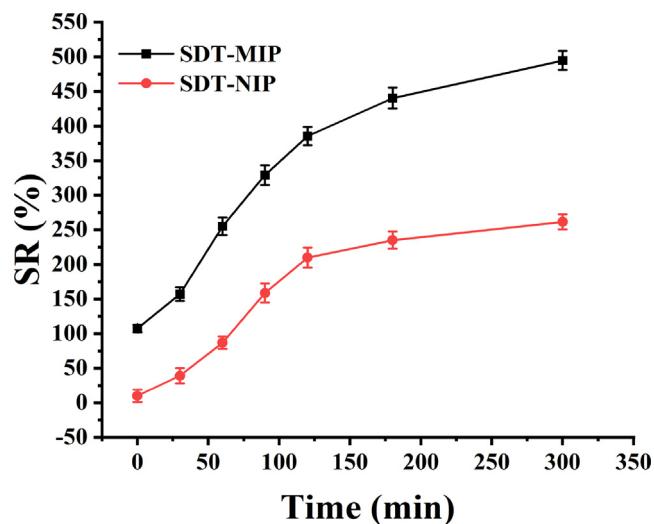


Fig. 6 The swelling ratio of SDT-MIP and SDT-NIP (25 °C, pH = 7).

Therefore, it can be inferred that the sustained-release effect of SDT-MIP in the animal intestine is superior to that in the stomach.

3.7. Release pharmacokinetic analysis

Table 3 presents the relevant parameters of the zero-order kinetic model, first-order kinetic model, Higuchi's plane diffusion equation, and K-P kinetic equation for SDT-MIP and SDT-NIP under different pH conditions. The results revealed

Analytes	Linearity ($\mu\text{g/mL}$)	Regression equation	R^2	LOD ($\mu\text{g/mL}$) ($n = 7$)	LOQ ($\mu\text{g/mL}$) ($n = 7$)
Solidroside	50–1000	$y = 0.1174x + 0.0491$	0.9999	3.0007	10.0022

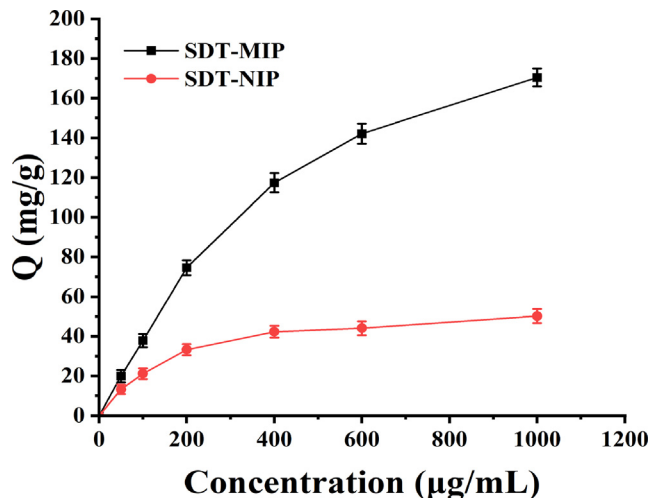


Fig. 7 Adsorption amounts of SDT-MIP and SDT-NIP (25 °C, pH = 7).

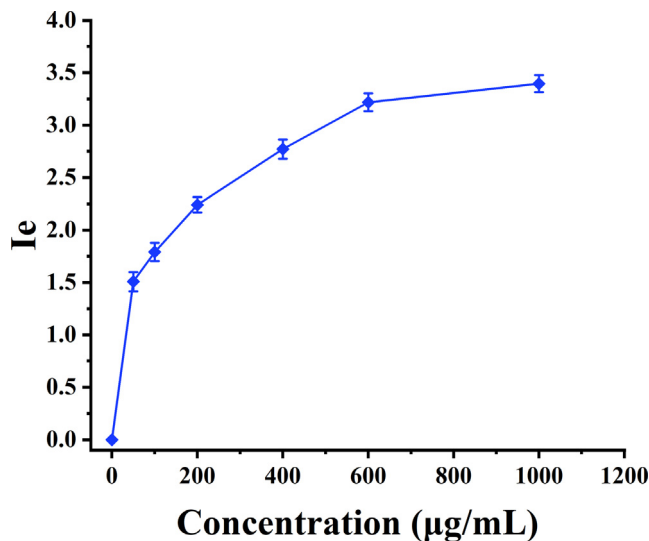


Fig. 9 Imprinting efficiency of SDT-MIP.

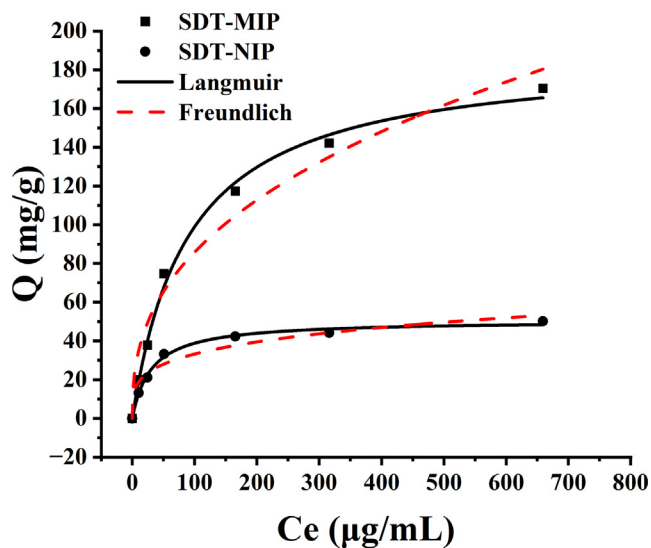


Fig. 8 Langmuir and Freundlich fit curves for SDT-MIP and SDT-NIP.

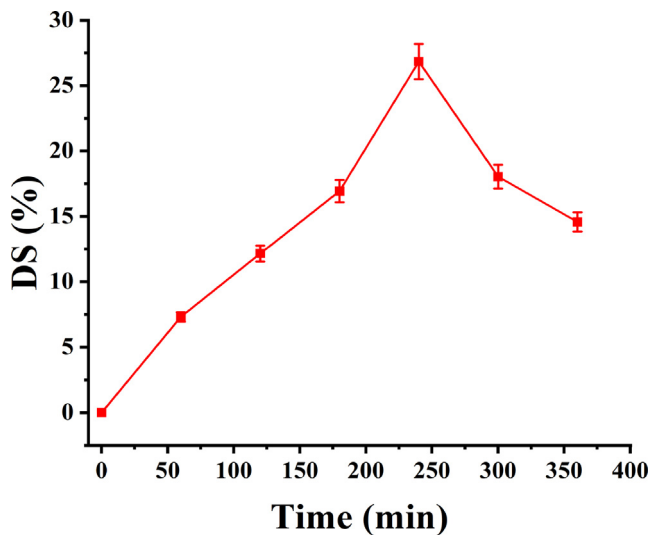


Fig. 10 Sustained release effect of SDT-MIP in AGF.

Table 2 Langmuir and Freundlich model constants and correlation coefficients.

Sample	Mode	K	A/n	R^2	Equation
SDT-MIP	Langmuir	188.24	90.16	0.9955	$Q = 188.24C_e / (90.16 + C_e)$
	Freundlich	14.02	0.39	0.9707	$Q = 14.02C_e^{0.39}$
SDT-NIP	Langmuir	50.65	30.48	0.9941	$Q = 50.65C_e / (30.48 + C_e)$
	Freundlich	10.56	0.25	0.9537	$Q = 10.56C_e^{0.25}$

that the SDT-MIP exhibited less effective fitting to the zero-order kinetic equation and first-order kinetic equation ($R^2_{pH=2} = 0.9793$, $R^2_{pH=7} = 0.9194$), indicating a nonlinear mechanism of drug release. Conversely, SDT-NIP showed good fitting to both zero-order and first-order kinetic equations at pH = 2 ($R^2 > 0.99$). Regarding Higuchi's diffusion equation, the SDT-MIP showed a weak fit, while the SDT-NIP showed some correlation ($R^2_{pH=2} = 0.9434$, $R^2_{pH=7} = 0.9684$). Discrimination was carried out based on the drug release index n in the K-P kinetic equation. At pH = 2

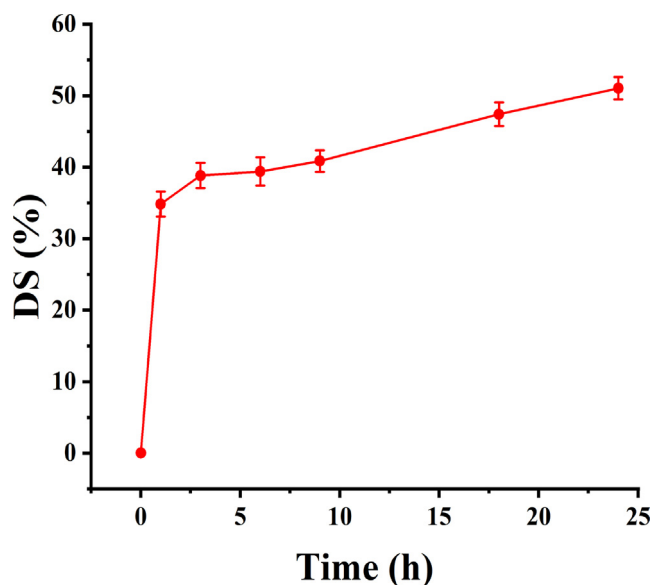


Fig. 11 Sustained release effect of SDT-MIP in AIF.

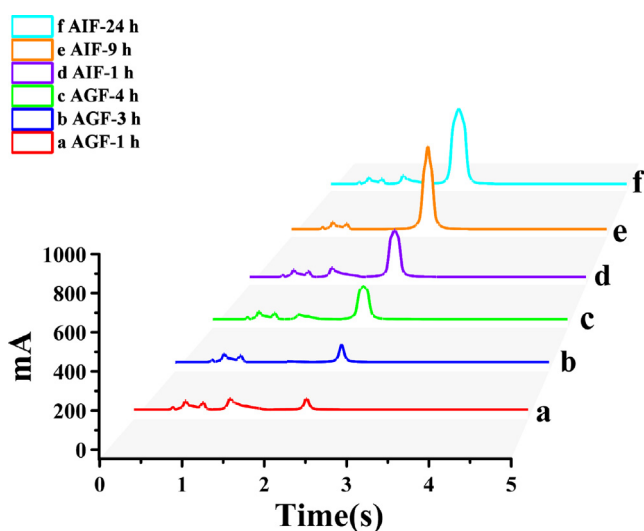


Fig. 12 HPLC detection results of SDT-MIP in AIF and AGF at different times.

and $\text{pH} = 7$, SDT-MIP exhibited a pure Fick diffusion mechanism ($n = 0.37$; $n = 0.12$), while SDT-NIP exhibited a combination of diffusion and framework dissolution mechanisms ($n = 0.65$) at $\text{pH} = 7$ and irregular diffusion ($n = 0.98$) at $\text{pH} = 2$. According to Fick's first law (Vidinha et al., 2022), the diffusion coefficients ranged from $3.38 \times 10^{-3} \text{ cm}^2/\text{s}$ to $2.78 \times 10^{-2} \text{ cm}^2/\text{s}$. The authors speculated that this difference was due to the complete dissolution of the framework under acidic conditions (Fangfang et al., 2022, Yi et al., 2022).

3.8. Effects on cell viability

Cytotoxicity testing was conducted, and the results are presented in Fig. 13. Cell viability analysis using the CCK-8 assay is shown in Fig. 14. The results indicate that TiO_2 , ranging from 0 to 1000 $\mu\text{g}/\text{mL}$, exhibited a cell survival rate of over $120 \pm 12.46\%$ in the presence of SDT-MIP solution. This

Table 3 The drug release kinetic model parameters.

Sample	pH	Zero-order		First-order		Higuchi		Ketger-Peppas		Release mechanism
		Equation	R^2	Equation	R^2	Equation	R^2	Equation	R^2	
SDT-MIP	2	$D_t = 2.85 t + 5.14$	0.5256	$D_t = 63.64(1 - e^{-0.02t})$	0.9793	$S_t = 1.07 t^{1/2} + 0.83$	0.6103	$D_t = 10.40 t^{0.37}$	0.6895	Fickian
	7	$D_t = 1.28 t + 24.90$	0.4786	$D_t = 43.71(1 - e^{-1.53t})$	0.9194	$S_t = 8.15 t^{1/2} + 15.89$	0.6518	$D_t = 33.35 t^{0.12}$	0.9893	Fickian
SDT-NIP	2	$D_t = 1.37 t + 0.39$	0.9908	$D_t = 71.47(1 - e^{-0.04t})$	0.9943	$S_t = 7.48 t^{1/2} - 3.14$	0.9434	$D_t = 1.68 t^{0.98}$	0.9926	Anamelous
	7	$D_t = 0.86 t + 2.11$	0.9533	$D_t = 26.11(1 - e^{-0.07t})$	0.9958	$S_t = 7.31 t^{1/2} - 4.16$	0.9684	$D_t = 2.36 t^{0.65}$	0.9844	Backbone corrosion

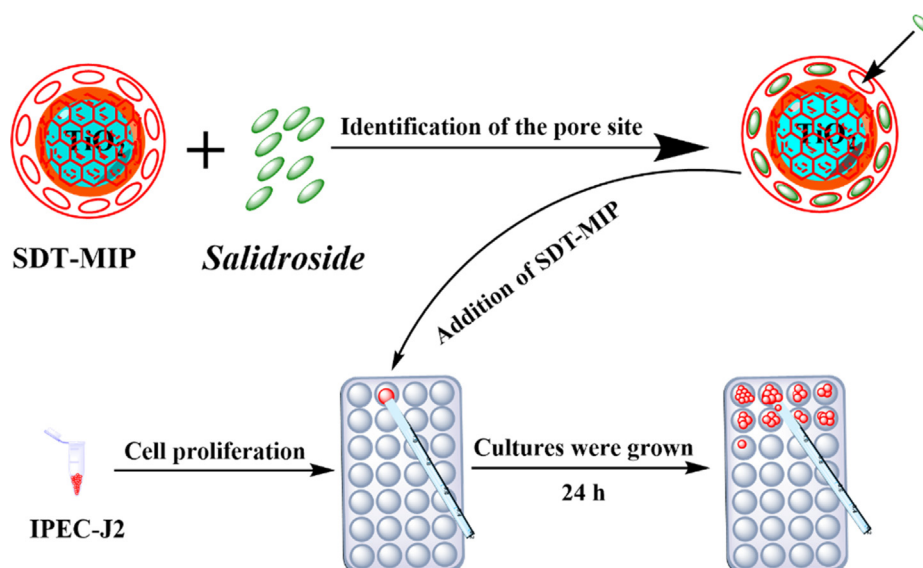


Fig. 13 Cytotoxicity assessment process of SDT-MIP.

demonstrates that TiO_2 is nontoxic and does not hinder cell growth, affirming its safety as a drug carrier. Salidroside at $600 \mu\text{g/mL}$ exhibited minor inhibitory effects but did not have an overall impact on cell viability. The effects of SDT-NIP at different concentrations on cell viability were comparable to those of TiO_2 , indicating that the synthesis method is safe, with TiO_2 being the only chemical involved in the synthesis that may impact cell growth. In contrast, SDT-MIP exhibited some growth-promoting effects on cells at various concentrations, and the cell activity increased as the concentration of SDT-MIP increased. The slow-release effect of SDT-MIP slowly releases salidroside and maintains the cells at an acceptable drug concentration environment, which is likely the reason for their growth-promoting effect. These results demonstrate the successful synthesis of SDT-MIPs and their potential as a drug carrier with a slow-release effect.

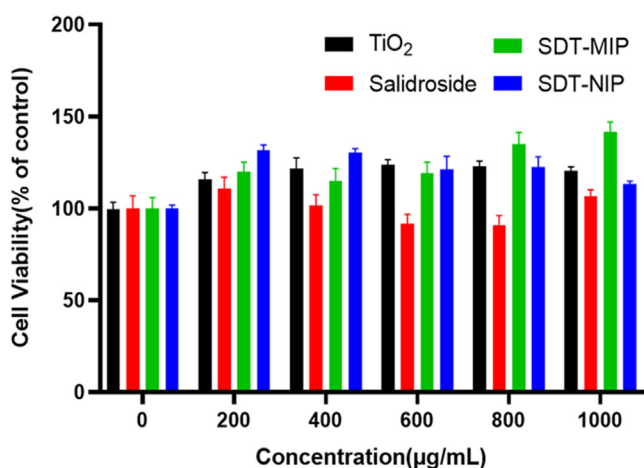


Fig. 14 Effect of TiO_2 , salidroside, SDT-MIP, and SDT-NIP on IPEC-J2 cell viability.

4. Conclusions

In summary, the SDT-MIP possesses molecular-specific recognition capabilities that enable the recognition and enrichment of salidroside. The proposed HPLC method demonstrated a favorable sustained release effect in intestinal fluid, following a pure Fick diffusion mechanism. Moreover, the study established the biocompatibility of SDT-MIP and its potential application in drug delivery. These findings provide valuable insights to support the development and utilization of sustained-release drugs.

CRedit authorship contribution statement

Zijie Liu: Methodology, Software, Formal analysis, Investigation, Resources, Data curation, Writing – original draft. **Xingbin Ma:** Conceptualization, Methodology, Resources, Data curation, Writing – original draft. **Shuyu Li:** Methodology, Formal analysis, Investigation. **Jiajie Qiu:** Formal analysis, Investigation. **Siyu Liu:** Formal analysis, Investigation. **Zhifeng Huang:** Investigation, Formal analysis. **Hongling Lin:** Validation, Investigation, Writing – review & editing. **A.M. Abd El-Aty:** Validation, Formal analysis, Writing – review & editing.

Declaration of Competing Interest

The authors declare that they have no known competing financial interests or personal relationships that could have appeared to influence the work reported in this paper.

Acknowledgments

This study was funded by a project supported by the Natural Science Foundation of Guangdong Province, China. (Grant No. 2022A1515010576), and the Project of Guangdong International, Hong Kong, Macao, and Taiwan high-end talent exchange program (NO. K21425), the Project of Enhancing School with Innovation of Guangdong Ocean University

[grant number: B20413/300702, B21129] and the Program for Scientific Research Start-Fund of Guangdong Ocean University [grant number: 101402/R20063].

References

- Abbas, O., Mehrorang, G., Maryam, A., et al, 2018. Hydrophilic multitemplate molecularly imprinted biopolymers based on a green synthesis strategy for determination of B-family vitamins. *ACS Appl. Mater. Interfaces* 10, 4140–4150.
- Al-Nemrawi, N., Hameedat, F., Al-Husein, B., et al, 2022. Photolytic controlled release formulation of methotrexate loaded in chitosan/TiO₂ nanoparticles for breast cancer. *Pharmaceuticals (Basel)* 15, 149–161. <https://doi.org/10.3390/ph15020149>.
- Bai, X.Y., Gao, W.K., Zhou, C.H., et al, 2022. Photoelectrochemical determination of diclofenac using oriented single-crystalline TiO₂ nanoarray modified with molecularly imprinted polypyrrole. *Microchim Acta.* 189, 90–99. <https://doi.org/10.1007/s00604-022-05206-8>.
- Bakhshizadeh, M., Sazgarnia, A., Seifi, M., et al, 2017. TiO₂-based mitoxantrone imprinted poly (Methacrylic acid-co-polycaprolactone diacrylate) nanoparticles as a drug delivery system. *Curr. Pharm. Des.* 23, 2685–2694. <https://doi.org/10.2174/1381612823666170214122413>.
- Bo, X., Ying, W., Xiaoyu, W., et al, 2012. Synthesis and characterization of N-(2-hydroxy)propyl-3-trimethyl ammonium chitosan chloride for potential application in gene delivery. *Colloids Surf. B Biointerfaces* 91, 168–174. <https://doi.org/10.1016/j.colsurfb.2011.10.053>.
- Cai, J., Dang, Q., Liu, C., et al, 2015. Preparation and characterization of N-benzoyl-O-acetyl-chitosan. *Int. J. Biol. Macromol.* 77, 52–58.
- Ceglowski, M., Kurczewska, J., Lusina, A., et al, 2022. EGDMA- and TRIM-based microparticles imprinted with 5-fluorouracil for prolonged drug delivery. *Polymers (Basel)*. 14, 1027–1041. <https://doi.org/10.3390/polym14051027>.
- Elkins, A.C., Deseo, M.A., Rochfort, S., et al, 2019. Development of a validated method for the qualitative and quantitative analysis of cannabinoids in plant biomass and medicinal cannabis resin extracts obtained by super-critical fluid extraction. *J. Chromatogr. B* 1109, 76–83.
- Fangfang, Z., Jingwei, M., Guangyan, T., et al, 2022. Preparation and characterization of furosemide solid dispersion with enhanced solubility and bioavailability. *AAPS PharmSciTech* 23, 65–76.
- Hasanzadeh Kafshgari, M., Kah, D., Mazare, A., et al, 2019. Anodic titanium dioxide nanotubes for magnetically guided therapeutic delivery. *Sci. Rep.* 9, 13439–13447. <https://doi.org/10.1038/s41598-019-49513-2>.
- He Lili, D.L., Yunzhu, L., 2013. Preparation and *in vitro* drug release properties of salidroside-chitosan nanoparticles. *Chin. Tradit. Herb. Drug* 44, 552–556.
- Jingjing, Z., Shijin, Z., Linqing, W., et al, 2022. The Antioxidant and antibacterial activities of the Pyridine-4-Aldehyde Schiff Bases grafted chloracetyl chitosan oligosaccharide derivatives. *Starch - Stärke* 75, 2100268–2100279.
- Karthika, V., Kaleeswaran, P., Gopinath, K., et al, 2018. Biocompatible properties of nano-drug carriers using TiO₂-Au embedded on multiwall carbon nanotubes for targeted drug delivery. *Mater. Sci. Eng. C Mater. Biol. Appl.* 90, 589–601. <https://doi.org/10.1016/j.msec.2018.04.094>.
- Karzar Jeddi, M., Mahkam, M., 2019. Magnetic nano carboxymethyl cellulose-alginate/chitosan hydrogel beads as biodegradable devices for controlled drug delivery. *Int. J. Biol. Macromol.* 135, 829–838. <https://doi.org/10.1016/j.ijbiomac.2019.05.210>.
- Kuei, S., Jen, et al, 2015. Interlayer grafting of kaolinite with N-(β-aminoethyl)-γ-aminopropyl trimethoxy silane. *J. Chin. Ceram. Soc.* 43, 1150–1155. <https://doi.org/10.14062/j.issn.0454-5648.2015.08.18>.
- Langmuir, I., 1916. The constitution and fundamental properties of solids and liquids. Part I. Solids. *J. Am. Chem. Soc.* 38, 2221–2295. <https://doi.org/10.1021/ja02268a002>.
- Lee, Y.H., Park, H.I., Chang, W.S., et al, 2021. Triphenylphosphonium-conjugated glycol chitosan microspheres for mitochondria-targeted drug delivery. *Int. J. Biol. Macromol.* 167, 35–45. <https://doi.org/10.1016/j.ijbiomac.2020.11.129>.
- Liang, Y., Zhao, Q., Liu, H., et al, 2019. Amido surface-functionalized magnetic molecularly imprinted polymers for the efficient extraction of Sibiskoside from *Sibiraea angustata*. *J. Chromatogr. B Analyt Technol. Biomed. Life Sci.* 1109, 90–98. <https://doi.org/10.1016/j.jchromb.2019.01.009>.
- Luo, M., Peng, H., Deng, Z., et al, 2015. Preparation and characterization of genipin-crosslinked chitosan microspheres for the sustained release of salidroside. *J. Int. J. Food Eng.* 11, 323–333.
- Ma, X., Lin, H., Zhang, J., et al, 2018. Extraction and identification of matrine-type alkaloids from *Sophora moorcroftiana* using double-templated molecularly imprinted polymers with HPLC-MS/MS. *J. Sep. Sci.* 41, 1691–1703. <https://doi.org/10.1002/jssc.201701133>.
- Ma, X., Lin, H., He, Y., et al, 2019a. Magnetic molecularly imprinted polymers doped with graphene oxide for the selective recognition and extraction of four flavonoids from *Rhododendron* species. *J. Chromatogr. A.* 1598, 39–48. <https://doi.org/10.1016/j.chroma.2019.03.053>.
- Ma, X., Lin, H., He, Y., et al, 2019b. Magnetic molecularly imprinted polymers doped with graphene oxide for the selective recognition and extraction of four flavonoids from *Rhododendron* species. *J. Chromatogr. A* 1598, 39–48.
- Ma, X., Zhang, X., Lin, H., et al, 2020. Magnetic molecularly imprinted specific solid-phase extraction for determination of dihydroquercetin from *Larix griffithiana* using HPLC. *J. Sep. Sci.* 43, 2301–2310. <https://doi.org/10.1002/jssc.201901086>.
- Ma, X., Lin, H., Yong, Y., et al, 2022. Molecularly imprinted polymer-specific solid-phase extraction for the determination of 4-hydroxy-2 (3H)benzoxazolone isolated from *Acanthus ilicifolius* Linnaeus using high-performance liquid chromatography-tandem mass spectrometry. *Front. Nutr.* 9, 1–11. <https://doi.org/10.3389/fnut.2022.950044>.
- Ma, X., Li, S., Qiu, J., et al, 2023. Development of an Fe(3)O(4) surface-grafted carboxymethyl chitosan molecularly imprinted polymer for specific recognition and sustained release of salidroside. *Polymers* 15, 1187. <https://doi.org/10.3390/polym15051187>.
- Oh, S., Kang, T., Kim, H., et al, 2007. Preparation of novel ceramic membranes modified by mesoporous silica with 3-aminopropyltriethoxysilane (APTES) and its application to Cu²⁺ separation in the aqueous phase. *J. Membr. Sci.* 301, 118–125. <https://doi.org/10.1016/j.memsci.2007.06.006>.
- Salahuddin, N., Gaber, M., Elneaneaey, S., et al, 2021. Co-delivery of norfloxacin and tenoxicam in Ag-TiO₂/poly(lactic acid) nanohybrid. *Int J Biol Macromol.* 180, 771–781. <https://doi.org/10.1016/j.ijbiomac.2021.03.033>.
- Shang, B.B., Sha, J., Liu, Y., et al, 2011. Synthesis of a new chitosan derivative and assay of *Escherichia coli* adsorption. *J. Pharm. Anal.* 1, 39–45.
- Shklover, V., Nazeeruddin, M.K., Zakeeruddin, S.M., 1997. Structure of nanocrystalline TiO₂ powders and precursor to their highly efficient photosensitizer. *Chem. Mater.* 9, 430–439.
- Sohan, L., Sanjiv, A., Shikha, R., et al, 2020. Synthesis and characterization of water-soluble chitosan derivatives: spectral, thermal and biological studies. *J. Macromol. Sci. A* 57, 1–9.
- Vaneckova, T., Bezdekova, J., Han, G., et al, 2020. Application of molecularly imprinted polymers as artificial receptors for imaging. *Acta Biomater.* 101, 444–458. <https://doi.org/10.1016/j.actbio.2019.11.007>.
- Vidinha, H., Branco, R., Neto, M.A., et al, 2022. Numerical modeling of damage caused by seawater exposure on mechanical strength in fiber-reinforced polymer composites. *Polymers* 14, 3955. <https://doi.org/10.3390/polym14193955>.

- Wang, Y., Yang, X., Pang, L., et al, 2022. Application progress of magnetic molecularly imprinted polymers chemical sensors in the detection of biomarkers. *Analyst* 147, 571–586. <https://doi.org/10.1039/d1an01112j>.
- Wei, L., Zhang, J., Luan, F., et al, 2018. Synthesis, characterization, and the antifungal property of aminoethyl chitosan quaternary ammonium salts. *Starch Stärke*. 70, 1700266–1700273.
- Yi, L.-X., Fang, R., Chen, G.-H., 2013. Molecularly imprinted solid-phase extraction in the analysis of agrochemicals. *J. Chromatogr. Sci.* 51, 608–618. <https://doi.org/10.1093/chromsci/bmt024>.
- Yi, W., Wenchao, W., Endian, Y., et al, 2022. Preparation of a camptothecin analog FLQY2 self-micelle solid dispersion with improved solubility and bioavailability. *J. Nanobiotechnol.* 20, 402–417.
- Yuksel, N., Tektas, S., 2022. Molecularly imprinted polymers: preparation, characterisation, and application in drug delivery systems. *J Microencapsul.* 39, 176–196. <https://doi.org/10.1080/02652048.2022.2055185>.
- Zhang, X., An, D., Zhang, R., et al, 2022. Preparation of carbon nanotubes and polyhedral oligomeric-reinforced molecularly imprinted polymer composites for drug delivery of gallic acid. *Int. J. Pharm.* 615, 121476–121484. <https://doi.org/10.1016/j.ijpharm.2022.121476>.
- Zhang, C., Wang, Y., Zhou, Y., et al, 2014. Silica-based surface molecular imprinting for recognition and separation of lysozymes. *Anal. Methods* 6, 8584–8591.
- Zheng, T., Wang, W., Wu, F., et al, 2019. Zwitterionic polymer-gated Au@TiO₂ core-shell nanoparticles for imaging-guided combined cancer therapy. *Theranostics.* 9, 5035–5048. <https://doi.org/10.7150/thno.35418>.
- Zhengming, C., Guoqing, M., Mengqi, W., et al, 2023. Enhanced microwave absorption for high filler content composite molded from polymer coated flaky carbonyl irons modified by silane coupling agents. *J. Wuhan Univ. Technol. (Mater. Sci.)* 38, 42–51.
- Zhong, H., Xin, H., Wu, L.X., et al, 2010. Salidroside attenuates apoptosis in ischemic cardiomyocytes: a mechanism through a mitochondria-dependent pathway. *J. Pharmacol. Sci.* 114, 399–408. <https://doi.org/10.1254/jphs.10078fp>.
- Zhu, L., Liu, X., Wang, X., et al, 2019. Evaluation of photocatalytic selectivity of Ag/Zn modified molecularly imprinted TiO₂ by multiwavelength measurement. *Sci. Total Environ.* 703, 134732–134742.